Solid Freeform Fabrication 2023: Proceedings of the 34th Annual International Solid Freeform Fabrication Symposium – An Additive Manufacturing Conference
Reviewed Paper

Improving the Mechanical Response of the IWP Exo-skeletal Lattice Through Shape Optimization

Joseph W. Fisher[1,3], Simon W. Miller[3], Joseph Bartolai[3], Timothy W. Simpson[1,2]

[1]Department of Mechanical Engineering, The Pennsylvania State University, University Park, PA 16802
[2]Department of Industrial and Manufacturing Engineering, The Pennsylvania State University, University Park, PA 16082
[3]Applied Research Lab, The Pennsylvania State University, State College, PA 16803

Abstract

Triply Periodic Minimal Surfaces have been identified as good candidates for the generation of lattice structures produced with additive manufacturing. These TPMS-based lattice structures avoid sharp features that are characteristic of strut-based lattice structures because of their constant zero mean curvature. Although studies have explored part-scale optimization using TPMS-based lattice structures, they have only varied the volume fraction by changing the level set in the approximate surface equations. By defining new parameterizations in the approximate surface equation, we can redistribute volume within the lattice structure at any volume fraction. In this paper, we introduce an approach for optimization of this new parameterization of TPMS equations using the Borg multi-objective evolutionary algorithm. We demonstrate this framework on the IWP exo-skeletal lattice under uniaxial compression. A relationship between the new parameters and the level set is derived for designs on the Pareto frontier of the optimized IWP TPxS. The performance of the Pareto optimal designs and the efficacy of the optimization approach are shown by comparing to the standard IWP lattice and four other lattices that share the same topology. The optimized designs are implemented and shared in custom nTopology blocks.

Keywords: Lattice Structures, Triply Periodic Minimal Surface, Shape Optimization

1 INTRODUCTION

One of the major draws of additive manufacturing (AM) is that components can be redesigned to reduce weight with the same or improved performance by taking advantage of the design freedom offered by AM [1]. One method of reducing weight in parts designed for AM is by incorporating lattice structures into designs. Lattice structures, also known as lattices, are repeating three dimensional structures that can be used to fill regions of the component. These structures exist between the macro-scale structure of the component and the microstructure of the material, unlocking new design opportunities. A lattice offers the ability to generate regions that are not completely solid but retain a significant portion of the mechanical properties of the material it is made from, thus reducing the resulting part's weight [2, 3]. Many studies have proposed a large variety of different

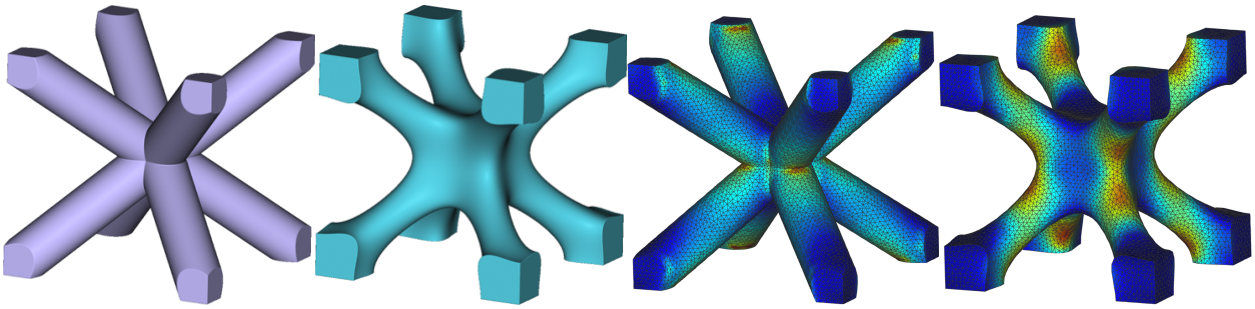

(a) (b) (c) (d)

Figure 1: Models of (a) the Body Centered Cubic (BCC) unit cell and (b) the I-graph–Wrapped Package graph (IWP) exo-skeletal (TPxS) lattices which share the same topology. Finite element analysis (FEA) of each lattice in uniaxial compression is presented in (c-d) with a 13% reduction in peak von Mises stress in the IWP TPxS compared to the BCC. The stress concentrations where struts in the BCC lattice intersect is avoided by the smooth curvature of the IWP TPxS. The boundary conditions and loads for the FEA are identical to those of the validation models which are given in Table 1

.

lattice topologies [e.g., 4, 5, 6]. Two classes of lattice structures have recently seen significant traction within the field, those based on struts and those based on Triply Periodic Minimal Surfaces (TPMS) [7]. A strut-based lattice is a three dimensional truss like structure composed of individual struts that join together at discrete nodes. One limitation of strut-based lattice structures is that the sharp intersections between struts result in stress concentrations. These concentrations can be minimized by applying rounds to the junctions, but this can be computationally expensive when the lattice structure has many members [8, 9]. TPMS-based lattices are modeled using approximate equations defined by 3D Fourier series fits of surfaces of zero mean curvature (minimal) that exhibit periodicity in $\mathbb{R}^3$ (triply periodic) [10]. By definition, a minimal surface cannot have sharp corners, as it would violate the zero mean curvature. This property reduces stress concentrations, allowing for better utilization of material. The majority of strut and TPMS lattice structures vary greatly from one another, however, the strut-based Body Centered Cubic (BCC) and TPMS-based I-graph–Wrapped Package-graph (IWP) exo-skeletal (TPxS) lattice structures share the same connectivity (See Figures 1a and 1b). As shown in Figures 1c and 1d, the IWP TPxS shows improvements to the mechanical properties compared to the BCC, which is consistent with Zhao et al. [11]. In addition, using a TPMS as a basis can be an efficient way to generate large and variable lattice structures [12].

The Fourier series fit used to model lattices based on the IWP TPMS, given in Equation 1, was derived by Von Schnering and Nesper [10]. In this work we use the following shorthand for the cosine function $C_{ni} = \cos\left(\frac{2\pi n}{d_i} i\right)$ where i is a spatial coordinate (i.e. x, y, z), d_i is the period of the lattice's unit cell in direction i, and n is the number of periods of the trigonometric function in one period of the lattice in direction i. (e.g. $1, 2$), when n is one, it is omitted simplicity.

$$2\left(C_xC_y + C_yC_z + C_zC_x\right) - 1\left(C_{2x} + C_{2y} + C_{2z}\right) = t \tag{1}$$

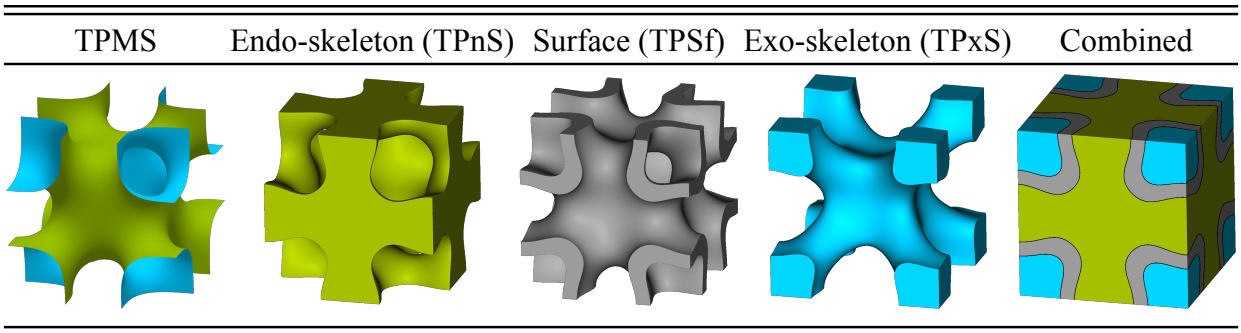

Figure 2: The IWP surface and the three types lattice structures modeled from it using Equation 1. Reproduced with permission from [13].

The two terms on the left hand side of Equation 1 define the surface that approximates the IWP TPMS, and t is a level set that provides an offset to that surface allowing the volume of material in the lattice to be changed.

Implicit equations that approximate TPMS, including Equation 1, can be used to model three unique types of lattice structures by defining solid material based on the value of the field in space. The three types are: the endo-skeleton (TPnS), the exo-skeleton (TPxS), and the surface (TPSf) [13]. Respectively, these three lattice structures are modeled by defining the following regions of the field as solid: less than t, greater than t, and those between t and $-t$. We show these three lattices for the IWP in Figure 2, highlighting the unique geometries. For this work, we focus on the TPxS.

For the discussion of lattice structures, we define the volume fraction as the volume of the solid material in the lattice normalized by the volume of the space that the lattice is filling. Lattice structures are often discussed in terms of their volume fraction in the literature as it provides a common basis for comparison between lattices that is independent of lattice topology and the geometry of the space that the lattice is filling.

The first two terms of Equation 1 can be inspected separately to understand the impact that each has on the topology of the resulting surface. Structures produced using each term alone are shown in Figure 3. Informally, we can say that the two terms respectively draw mass toward and away from the "nodes" of the lattice at the center and corner of the unit cell. If the second term in Equation 1 had a coefficient greater than one, the "nodes" would be smaller and the "beams" thicker. In Equation 1, the ratio of the two is fixed as 2:1, which provides a best fit to the IWP TPMS when $t = 0$ [10]. Since this equation was derived at a single level set (which is also a single volume fraction), and not based on any criteria specific to lattice design, it is likely that variation on Equation 1 can improve the performance of the lattice. With this motivation, we define a new equation with variables in place of the coefficients 2 and 1, shown below in Equation 2. We also define our first research question: **Can the response of the IWP TPxS lattice be improved at one or more volume fractions by varying the coefficients A and B present in its equation?**

$$A\left(C_xC_y + C_yC_z + C_zC_x\right) - B\left(C_{2x} + C_{2y} + C_{2z}\right) - t > 0 \tag{2}$$

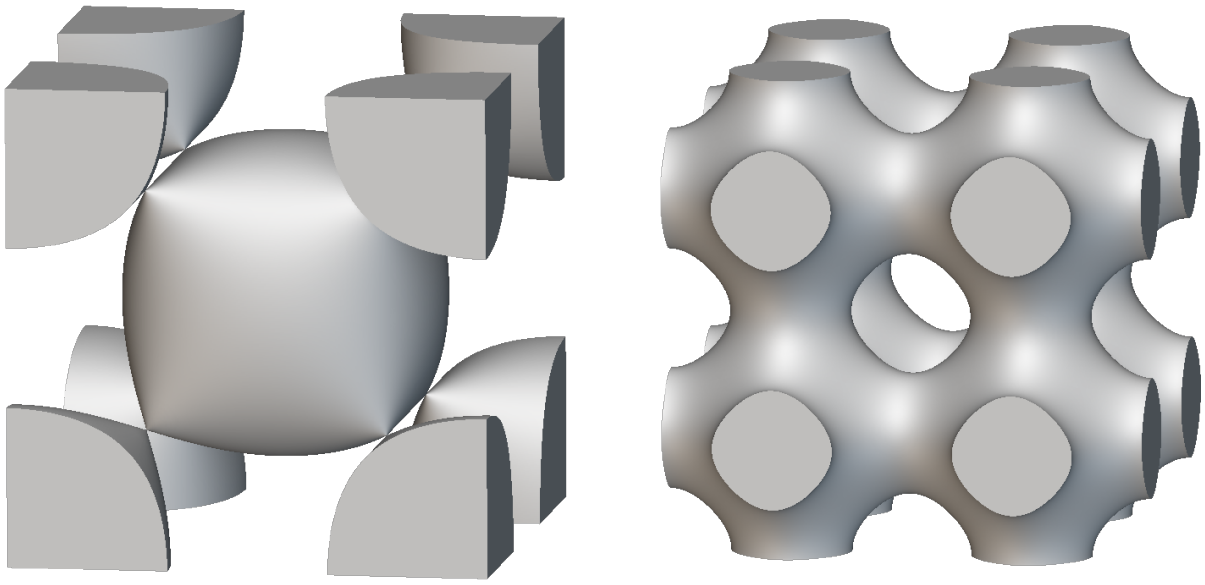

(a) **(b)**

Figure 3: Models generated with (a) the first and (b) second terms of Equation 1 in isolation. The balancing of the two terms provides a useful approximation of the IWP TPMS. Both terms show mirror symmetry in x, y, and z through the center of the unit cell.

The values of A, B, and t can be varied to generate unique structures, producing a 3D design space in which to search for optimal designs. The optimization of TPMS-based lattice structures has been performed at the component scale by changing value of the level set t to redistribute mass within the lattice to meet the performance requirements of the component [14, 15, 16]. In addition, the optimization of strut-based unit cells has appeared multiple times in the literature with different approaches. Ground structure approaches, utilizing a multi-objective evolutionary algorithm (MOEA), have been demonstrated for generating novel unit cells for specific applications [17]. Several optimizations have been performed on the BCC lattice to improve the response of the lattice. Wang et al. [8] approached the optimization by adding rounds to the intersection of the struts whose radius was a function of the strut radius. Lee, Zhang, and Gu [18] applied a machine learning approach to optimize the profile of the struts which they parameterized as 30th order Bézier curves. Zhao et al. [19] defined the BCC lattice using struts that have a hexagonal cross-section that taper linearly from the nodes to the center of the beam. This approach reduces the complexity of the model, replacing curved surfaces with trapezoidal faces that are more easily meshed; however, this approach does result in different stress concentrations at the mid-span of the struts where the planer faces intersect. We show examples of the geometry generated using these three approaches in Figure 4. When discussing these different lattices in this work, we will reference them by the last name of the first author (i.e. Wang, Lee, and Zhao). These three optimizations of the BCC lattice all included uniaxial compression as a load case in their optimization, giving a common point of comparison. This leads to a second research question: **Do the results of optimization of the IWP TPxS outperform optimizations of the BCC lattice which share the same topology?** For TPMS-based lattices, no studies have performed this type of optimization on the unit cell prior to utilizing it at the component scale. As demonstrated by prior works (e.g., [8]), such an optimization

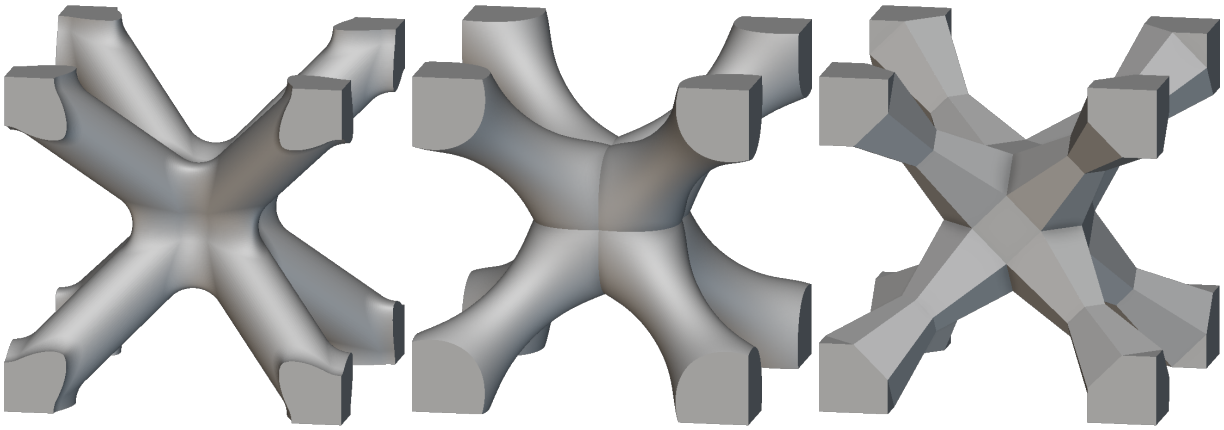

(a) **(b)** **(c)**

Figure 4: Optimized BCC unit cells from (a) Wang et al. [8], (b) Lee, Zhang, and Gu [18], and (c) Zhao et al. [19] at volume fractions of 0.1970, 0.2409, and 0.1977, respectively. The smooth curvature of (b) shows a strong similarity to the IWP TPxS; however, creases at the intersections of the struts persist through the optimization that lead to stress concentrations.

can increase the performance of the lattice structure. In the new parameterization in Equation 2, the coefficients A, B, and the parameter t can be used as inputs for the optimization of the lattice since they are not fixed values. Unit cells that have been optimized can then be utilized in component level optimization. In addition to other optimizations including uniaxial loading cases, the majority of lattice structure analysis and mechanical testing is performed in uniaxial compression [20, 4, 16]. For consistency, we target the same loading conditions. By applying periodic boundary conditions, we can approximate the response of an infinite lattice using a single unit cell [21].

The BCC optimizations mentioned previously resulted in geometry that is defined either for any volume fraction or for only discrete volume fractions. Specifically, Wang et al. [8] and Zhao et al. [19] developed mathematical relationships which can be used to model lattices at any volume fraction, where Lee, Zhang, and Gu [18] developed lattices only at discrete volume fractions. The former of these two is advantageous because they can be used to smoothly transition between different volume fractions when performing part scale optimization as demonstrated by [22, 8, 15]. Comparing these types of results motivates an additional research question: **Do relationships between the optimal coefficients at different volume fractions exist, leading to a reduction of parameters?**

For each research question, we hypothesize the results below.

RQ1: *Can the response of the IWP TPxS lattice be improved at one or more volume fractions by varying the coefficients A and B present in its equation?* We hypothesize that lattice performance can be improved, and at all volume fractions, by changing the weighting of A and B with an appropriate selection of t.

RQ1.1: *Do relationships between the optimal coefficients at different volume fractions exist, leading to a reduction of parameters?* We hypothesize that such relationships exist

between coefficients of true Pareto-optimal solutions, but the recovery of such relationships is contingent on the objective evaluation approach and optimality criteria. We note that optimization can only *approximate* the Pareto frontier [23, p. 17], so any relationships we find between coefficients will depend on this approximation.

RQ2: *Do the results of optimization of the IWP TPxS outperform optimizations of the BCC lattice which share the same topology?* As we have shown (for a single volume fraction) the IWP TPxS out performs the BCC lattice in uniaxial compression (see Figure 1) and we hypothesize that optimization of the IWP TPxS will outperform optimization of the BCC provided both maintain the same topology.

To answer these questions, we have developed a method of optimizing the unit cells of the IWP TPxS lattice. In Section 2, we present the definition of the design space and the problem definition; we then define the objective function and the method we use to evaluate it before discussing the selection of our optimization scheme. In Section 3, we evaluate relationships between the Pareto-optimal designs and compare the Pareto-optimal lattices to existing lattices and discuss our research questions. We then apply homogenization approaches to study the lattice performance and anisotropy before summarizing our work and discussing possible extensions in Section 4.

2 METHODS

In this section, we outline our approach to defining out optimization problem, the optimization method employed, and the implementation of the methods.

2.1 Design Space & Problem Definition

The design space for our optimization problem is a real three dimensional space consisting of the parameters A, B, and t from Equation 2. We bound this space to a right rectangular prism by defining the following inequality constrains:

$$0 \leq A \leq 1 \tag{3}$$

$$0 \leq B \leq 1 \tag{4}$$

$$-1 \leq t \leq 1 \tag{5}$$

Negative values of A or B were found to produce topologically distinct structures that do not share connectivity with the IWP TPxS. Therefore, we consider only positive values. Not all designs within the space defined by Equations (3) to (5) are valid. To fully define the feasible region of the design space, we first evaluate Equation 2 over a linearly-spaced 3D grid of 128,000 designs (a $40 \times 40 \times 80$ grid). We evaluated each point for two criteria: connectivity and topology. To test connectivity, each design Equation 2 is evaluated over a 3D grid in x, y, z space. Taking a level set of this grid at t, we apply Lewiner's Marching Cubes algorithm to define the surface of the lattice geometry as a triangular mesh [24]. The faces of this mesh are then used to construct an undirected graph. If all vertices of this graph are connected, the geometry of the design is connected also. We

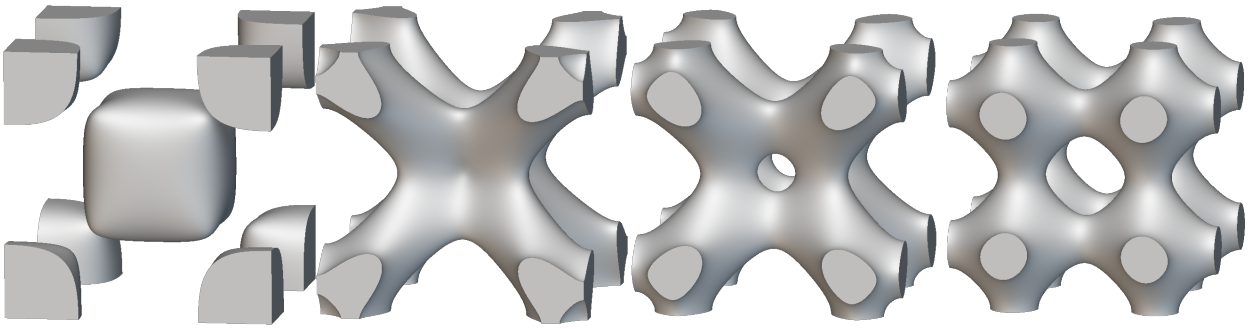

(a) (b) (c) (d)

Figure 5: Example structures that are possible outside the feasible region. (a) a design that is discontinuous, and (b-d) connected designs with whose topology is inconstant with the IWP TPxS, because the second term of Equation 2 dominates to an increasing degree. The structure in (b) has internal voids at both the center and corners of the unit cell.

note that this is not universally true for all unit cells of all TPMS-based lattices, such as the common unit cell of the gyroid which appears to have disconnected volume "floating" in the corners [13]. However, the "floating" volumes in the gyroid connects to the rest of the structure through adjacent unit cells. For the lattices of the IWP surface, the volume remains connected inside the unit cell, so the connectivity check described previously can be applied. To test the topology of the lattice, we evaluated Equation 2 at a corner point of the unit cell. To match the desired topology this point must fall within the lattice. Examples of four designs that fall outside the feasible region are shown in Figure 5.

For valid designs, we evaluated two metrics of interest: volume fraction and minimum hydraulic diameter of the "beams" using Equation 6. Where A_c and p are the cross-sectional area and perimeter of the "beam" at the mid-span of the "beam". We evaluated A_c and p using the surface mesh generated using the Marching Cubes algorithm. The hydraulic diameter is used in Section 2.1.2 to highlight the variation between the geometry of different valid designs independent of volume fraction.

$$d_h = 4\frac{A_C}{p} \tag{6}$$

The design space was visualized using the ARL Trade Space Visualizer[1] [25] to plot each valid design as a cube colored by the volume fraction of the design (see Figure 6). The design space is an irregular octahedron, five of whose faces are already defined by Equations (3) to (5). Constraints for the remaining three faces were defined using the equation of a plane in 3D, commonly expressed as:

$$ax + by + cz - d = 0 \tag{7}$$

where x, y, and z are the design variables A, B, and t, respectively. We compute the coefficients a, b, c, and d for each of the three surface using a modified version of the MATLAB function

[1] http://www.atsv.psu.edu/whatisatsv.html

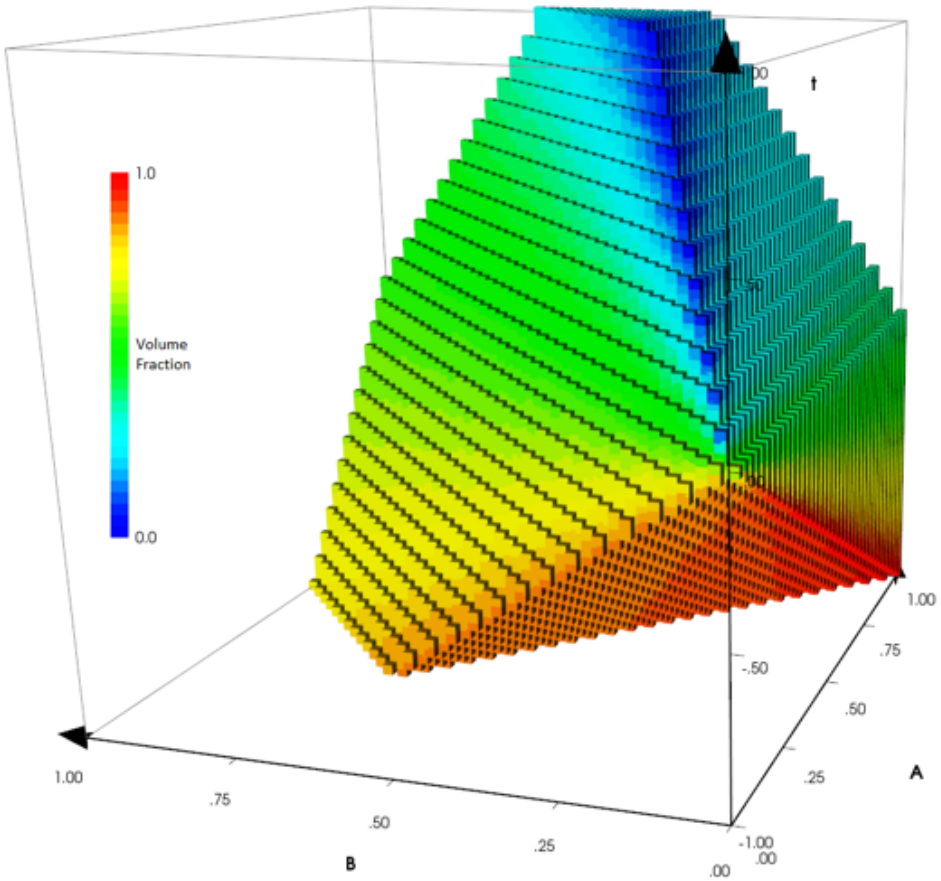

Figure 6: Exploration of the 3D design space resulted in a polyhedron with 8 faces representing the feasible region (Ω). Color indicates the volume fraction which is the percentage of the lattice unit cell that is solid.

`plot_plane` [26] and three noncollinear design points on each face of the domain. The coefficients a, b, and c respectively are the A, B, and t components of the plane's unit normal, and d is the offset from the origin in the direction of the normal. The constraints derived for the three faces are:

$$-0.24A + 0.24B + 0.08t + 0.0010 \leq 0 \tag{8}$$

$$-0.45B + 0.15t - 0.0019 \leq 0 \tag{9}$$

$$0.21A + 0.21B - 0.22t + 0.0027 \leq 0 \tag{10}$$

The feasible region of the design space (Ω) for our optimization is defined using the inequalities of Equations (3) to (5) and (8) to (10).

2.1.1 Scalability of Design Space

The standard definition of the IWP equation uses $A = 2$, and $B = 1$, and t ranges from -5.0 to 3.0 [13]. Because the multiplicative property of equality applies to implicit equations like Equation 1, the standard designs are within the feasible region Ω, even though the feasible region is defined on the scale of unity.

2.1.2 Independence of A and B

Wohlgemuth et al. [27] explored the variation of surfaces by varying the coefficients of terms in several implicit equations, including in Equation 2. When implementing Equation 2 the authors fixed $t = 0$ and applied the relationship $B = 1 - A$ to reduce the number of parameters to one. They then varied A from zero to one to study the changes to the surface topology. Applying the same relationship to our 3D design space, we once again considering the multiplicative property of equality to show that we can scale any values of A, B, and t by a common factor such that A and B satisfy the relationship $B = 1 - A$ without changing the geometry of the lattice. As a result, the design space can be reduced to a 2D space with A (or B) and t. However, for reasons discussed in Section 3.1, we found that giving the optimizer independent control over A and B was preferable so we maintain three dimensions in the design space of our study.

2.2 Definition and Evaluation of Objectives

For a given volume fraction, we seek to produce the stiffest version of the lattice possible. To this end, we consider two objectives. First, maximize the stiffness in the direction of compression (E_{11}), which we redefine as: minimize the reciprocal of the stiffness in the direction of compression. Second, minimize the volume fraction (VF). These two objectives will produce a Pareto frontier of designs each of which, within the limits of the convergence criteria (discussed in Section 2.4), will be the stiffest for that volume fraction. We apply two additional inequality constraints to the problem on the volume fraction objective, limiting the volume fraction to the range of [0.1, 0.9]. This lower limit avoids thin features that fail to mesh well, and this upper limit was imposed to prevent excessive evaluation time spent on designs that are not of particular interest to the authors. We now formulate the optimization problem as:

$$\begin{aligned} \min_{A,B,t} \quad & (1/E_{11}, VF) \\ \text{s.t.} \quad & \Omega \\ & 0.1 \leq VF \leq 0.9 \end{aligned} \tag{11}$$

To evaluate the first objective function, we use a linear finite element model using a voxel meshing approach based on Dong, Tang, and Zhao [21]. This is a computationally efficient approach that can be used to generate a highly regular volume mesh directly from an implicit equation without first extracting a surface mesh from the field. The voxel mesh is used to generate a mesh of constant strain three dimensional eight node (C3D8) brick elements. The Young's modulus (E) of each element is linearly weighted based on the number of nodes (n) of that element that are inside the lattice using Eq. 12.

$$E_{element} = E_{material} \frac{n}{8} \tag{12}$$

For the optimization, we aim to simulate the far field response of the lattice, not that of only a single, isolated unit cell [5]. When performing physical testing of lattices, a minimum of 64 cells

(in a 4x4x4 grid) is required to effectively eliminate edge effects [28]. However, in linear elastic simulation, we can take advantage of the periodic nature of the unit cell, by applying additional boundary conditions, to reduce the size of the model to a single unit cell of the lattice. The IWP TPxS has a cubic crystalline structure (like the BCC), which is a subset of orthotropic materials that, in addition to containing three orthogonal planes of symmetry [21], are invariant to 90° rotations of the lattice. Thus, we would require only three simulations to compute the three values needed to generate the homogenized constitutive matrix. Because we are only interested in minimizing the compliance of the lattice in one direction, the constitutive matrix is not expressly required. We therefore further reduce the computational load by evaluating the response of the lattice in only one load case which yields the first column of the constitutive matrix C. Because we do not calculate the full matrix, we cannot invert it to find the stiffness matrix, and we instead calculate an effective normalized stiffness in the direction of the compression load using Hooke's law solved for the elastic modulus given in Equation 13 and use in the first objective in Equation 11:

$$E_{11_{\text{eff}}} = \frac{\sigma_{11}}{d_\varepsilon C_{11}} \tag{13}$$

where σ_{11} is the (1,1) element of the stress tensor, d_ε is the applied displacement, and C_{11} is the (1,1) element of the constitutive matrix. We calculate the reciprocal of $E_{11_{\text{eff}}}$ to get our objective function, which we note is an analog for compliance as it was not generated using the full matrix.

For the IWP lattices, the faces of the unit cell, shown in Figure 1b, are also planes of symmetry. To account for the additional cells of the lattice that are not modeled, the nodes on the face of the cubic unit cell are restricted to move in the plane of the given face, to enforce symmetry, with the exception of nodes on the $x = P_x$ face which have a fixed, uniform displacement in the $-x$ direction. We use an isotropic material model with Young's modulus and Poisson's ratio of 2 GPa and 0.394, respectively.

When validating the results of the optimization and comparing against other lattice designs that share the same topology, the boundary conditions and performance metric are different from those described above. The validation model setup is presented in Section 2.5 and both the optimization and validation model setups are summarized in Table 1.

We note that because of the form of Equations 1 and 2, and the resulting rotational symmetry of the cubic crystal unit cell of the lattice, the response to a given loading in the y or z direction will always be the same as in the x direction. While this likely limits how much improvement in the x direction we can achieved, it results in a lattice that is more useful in application. Future work can explore the effects of allowing direction changes to the lattice geometry.

To evaluate the second objective, we compute the value of Equation 2 over a 3D grid in x, y, z space with 200 points in each direction, The number of points inside the lattice (points where Equation 2 ≤ 0) is divided by the total number of points in the unit cell to calculate the volume fraction.

Table 1: Summary of boundary conditions applied to FEA models for optimization runs and validation runs that are introduced in Sections 2.2 and 2.5, respectively. The two models use different boundary conditions at the $x = P_x$ surface of the unit cell as well as different criteria to measure the performance of the model due to differences in software capability. We use Δ to signify the prescribed displacement in the stated direction.

Boundary Conditions		
Boundary	Optimization Runs	Validation Runs
$x = 0$	$\Delta x = 0$	$\Delta x = 0$
$y = 0$	$\Delta y = 0$	$\Delta y = 0$
$z = 0$	$\Delta z = 0$	$\Delta z = 0$
$x = P_x$	$\Delta x = -0.01 P_x$	Fixed load in $-x$ direction distributed across surface
$y = P_y$	$\Delta y = 0$	$\Delta y = 0$
$z = P_z$	$\Delta z = 0$	$\Delta z = 0$
	Model Performance Criteria	
	$1/E_{11}$	Maximum nodal displacement

Per RQ1.1, the designs on the Pareto frontier will be related to one another in the design space such that the coefficients A and B can be defined as functions of t, allowing us to produce an equation with a single input parameter, similar to other TPMS-based lattice designs; however, the voxel approach we use to evaluate the objective function results in discrete steps in the performance space, making the derivation of these relationships more challenging.

2.3 Selection of Optimization Algorithm

In this work, we use the Borg MOEA to solve our optimization problem defined in Eq. 11. prior to applying Borg to this problem, two other optimization approaches were tested. First, we explored gradient based methods. These methods are compelling for this work because it was expected that they would result in a smooth Pareto frontier from which design space relationships could be derived. However, the voxel FEA approach used for expedient meshing and analysis does not produce locally smooth gradients in the performance space. Because these methods rely on the slope of the gradient to converge, they could not be used. Next we explored purely genetic approaches, the results of these optimization runs indicated that these approaches were not appropriate, as some designs on the Pareto frontier failed to outperform the standard equation (which is within the design space). This lead to the exploration of MOEAs that could adapt to the problem, and the selection of Borg. Borg is a high performance adaptive algorithm that was developed to solve difficult multi and many objective optimization problems and was selected because its auto-adaptive search features resolved issues with tuning the other algorithms considered [29].

2.4 Implementation

In this section we briefly describe details pertaining to the implementation of Borg and the function it calls for evaluation of the objectives. When Borg makes a call, it first evaluates the feasibility of

the design by computing the validity of each constraint and the distance from the constraint surface to the design, which is returned to Borg. If one or more constraints were violated, the analysis is bypassed, and the objective functions are returned to Borg as artificially high values $\left(\text{i.e.}\, 10^{20}\right)$, because Borg always expects real values to be returned.

When Borg was called, we used a maximum number of iterations of 100,000 and ε values of 0.01 for both objectives. The epsilon values effect both the density of designs on the Pareto frontier as well as the stagnation/convergence criteria of the algorithm. Respectively these are because Borg utilizes an ε-box dominance archive and an ε-progress method. Our epsilon values were selected because they produced a Pareto frontier of the desired density of approximately 1 design per 1% change in volume fraction.

Borg is available natively in both C and Python. The C implementation is more computationally efficient and offers wrappers to interface with other languages. The C implementation of Borg was compiled into a MATLAB executable allowing it to be called within MATLAB, allowing Borg to interface with existing meshing and analysis codes written natively in MATLAB.

The optimization was performed using MATLAB 2022a on a desktop workstation with an Intel Xeon W-2133 CPU and 128GB of RAM running Windows 10. Borg was run in series and the resources of the computer were not fully utilized, motivating parallel evaluation in future studies.

2.5 Validation Models

In order to evaluate the performance of our optimized lattice in comparison to existing designs in the literature, we first developed matching models to represent each using nTopology's internal analysis package. nTopology is able to natively model, mesh, and analyze lattices based on implicit equations, struts, and high order Bézier curves, allowing for easier integration and analysis which are used to model the IWP TPxS, BCC, and optimized BCC from Lee, Zhang, and Gu [18] respectively. Like other FEA tools, CAD models can also be imported for evaluation of the optimized BCC lattices from Wang et al. [8] and Zhao et al. [19].

The FEA was carried out using linear tetrahedral mesh elements that were generated by discretizing the surface of a given lattice model with triangles before populating the volume of the model uniformly with tetrahedrons. The unit cells were modeled as 10mm cubes, and the tetrahedrons were defined with an edge length between 0.1mm and 0.25mm depending on volume fraction and a fixed growth rate of 1.1 for all the models. The size of the triangles in the surface mesh were matched to that of the tetrahedrons to produce consistent element sizes at the surfaces of the model.

In addition to this change to the model setup, the validation models do not use the same performance metric. Instead, when validating the optimized structures against similar geometries from the literature, we use the maximum deflection of the model's nodes to quantify stiffness instead of calculating E_{11} using Equation 13. Table 1 shows the model setups for both the optimization and validation cases. While the differences between the two models means the results cannot be compared against each other, they can be used to compare to other lattice topologies that are analyzed with the same boundary conditions.

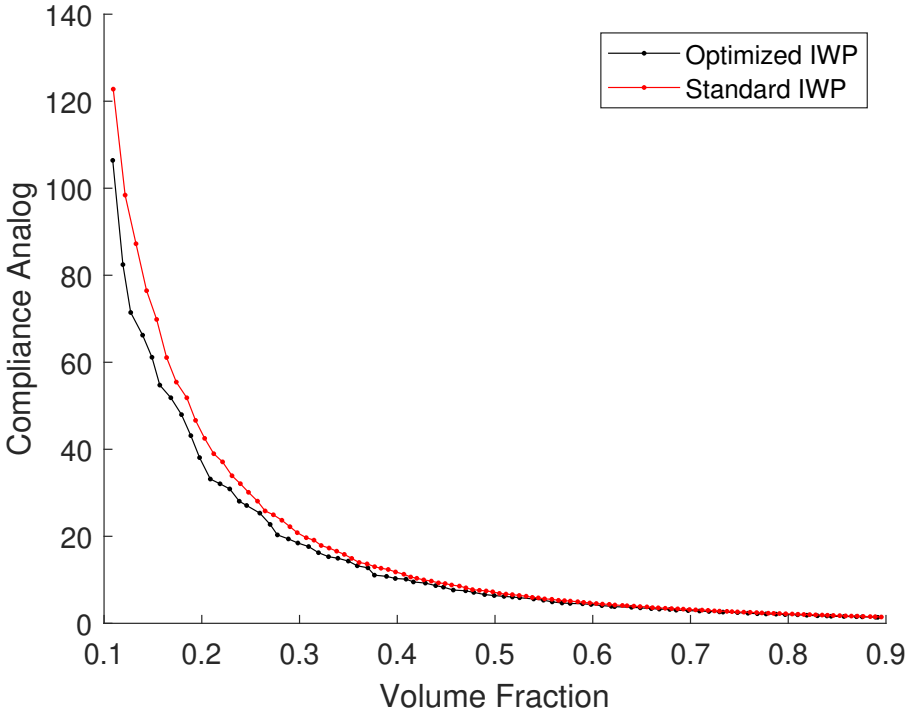

Figure 7: Borg output compared to standard IWP TPxS plotted in the performance space. Showing that the optimized structures outperform the standard across the range of volume fractions considered.

3 RESULTS

We present the Pareto frontier resulting from our Borg optimization in Figure 7. We also include the standard IWP TPxS in Figure 7, evaluated using the same model setup and solver to illustrate that the designs of the optimized version Pareto dominate those of the standard equation, answering RQ1. The optimization took 67 hours to converge within the limits given for the objectives, utilizing just over 85,000 evaluations, 72% of which fell within the feasible region.

To quantify the improvement of the optimized lattice over the standard IWP TPxS across the Pareto frontier, we evaluate the standard IWP TPxS was at 200 points, equally spaced in t-space. For each Pareto optimal design, the standard design from the dataset with the lowest volume fraction that was greater than that of the optimized volume fraction was used for comparison From this comparison the optimized design improves performance by between 2% and 18%. We tabulate these data in Appendix A for the 80 Pareto optimal IWP TPxS designs.

3.1 Relationships in the Design Space

We now seek empirical relationships between A, B, and t for the Pareto optimal designs in the design space. In Figure 8, we plot A and B as functions of t and no relationship between A and t or B and t were found when considered independently. Both A and B vary across the range of t values with only a slight trend to the data. Initial curve fits that included all points shown in Figure 8 resulted in designs that performed worse than the standard IWP TPxS. 3D visualization

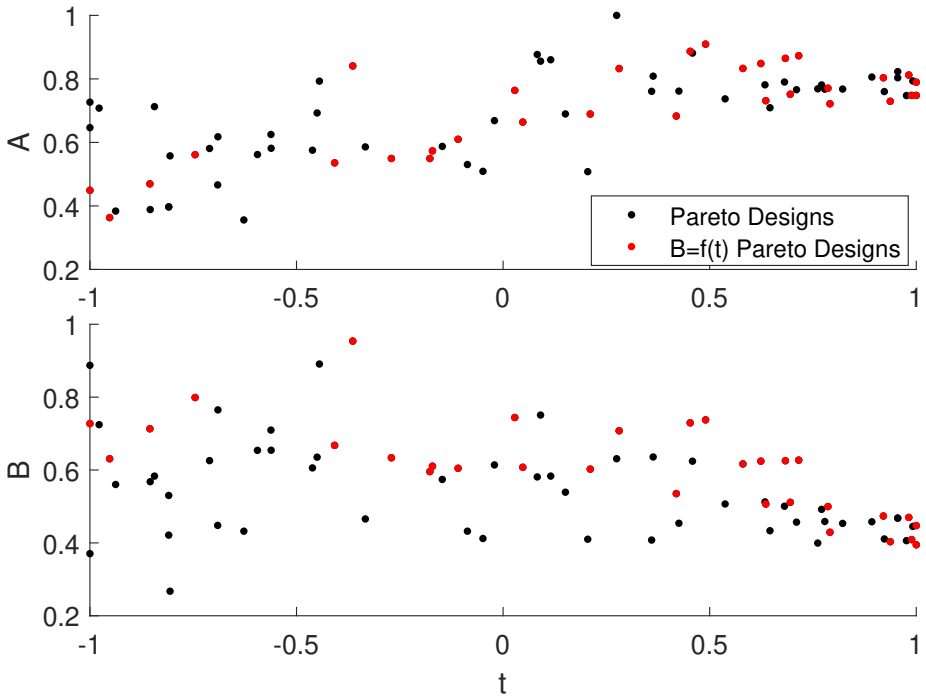

Figure 8: The A and B parameters of the designs on the Pareto frontier plotted as functions of the level set t. The designs in red are a subset of the Pareto frontier which are scaled and fit with a polynomial shown in Figure 10.

of the design space in Figure 9 illustrated that a relationship between A, B, and t for some, but not all, of the points on the Pareto frontier was likely to exist. To derive a relationship, we again invoked the multiplicative property of equality and normalized the parameters of each design such that $A = 2$. After normalizing, in Equation 14 we plot the scaled B values against the scaled t values. In this scaled B–t space, the data follow a generally linear trend, the spread of which is significant. When fit, this results in under-performing designs. We note that in this space the designs exhibit a distinct upper bound that is of interest. To identify points on this edge, we apply the concept of Pareto optimally to the existing designs in this B–t space, with the objective of maximizing B and t. These points are marked in red in both Figures 8 and 10. We then fit the second-order polynomial presented in Equation 14, plotted in red in Figure 10.

$$B_{\text{scaled}} = -0.007046t_{\text{scaled}}^2 - 0.322t_{\text{scaled}} + 1.972 \tag{14}$$

We now use the fixed value of A and the scaled $B = f(t)$ relationship with Equation 2 to model lattice structures. We analyze the designs on this curve using the same model setup and solver in as the optimization, and in Figure 11 we plot them with the optimized and standard IWP TPxS designs. We find that the designs generated with the curve fitting are distinct from the Pareto optimal designs found using Borg. The curve fit designs Pareto dominate all of the standard designs, but do not Pareto dominate any of the Borg optimized designs, answering RQ1.1. We therefore provide two results from this work. First, 80 discrete designs that show improvement over the standard design with volume fractions ranging from 0.1 to 0.9 and second, a new single variable

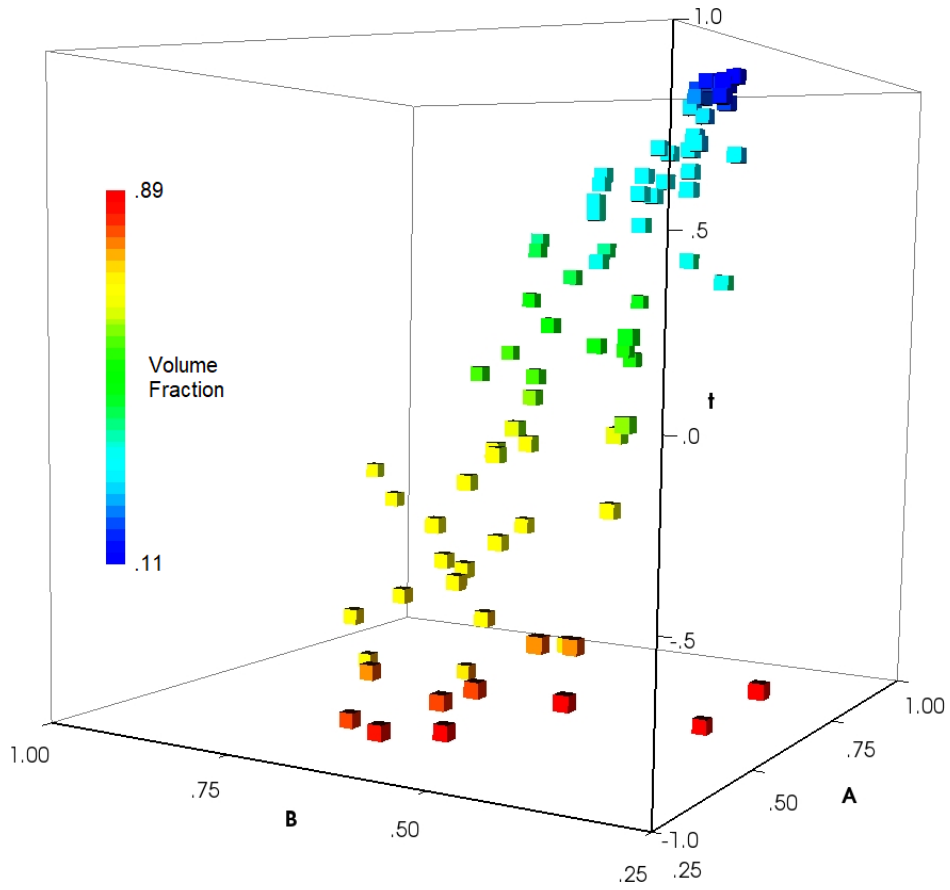

Figure 9: Pareto optimal designs plotted in the design space. A trend that involves A, B, and t can be seen. However, a 3D surface fitting of would not yield single value functions for A and B for a given value of t.

equation for modeling lattices which shows less improvement but is continuous. Both results have been packaged into custom nTopology blocks. These blocks make design and analysis of the lattices accessible and they can be downloaded from GitHub[2] under a Creative Commons Attribution 4.0 International License.

When applying this method to the Pareto frontier from the optimization run with two objectives we found that the points had no relationships that could be found and no significant differences between the frontier presented in this work and the two objective Pareto frontier. To avoid unnecessary confusion, we do not present the results of the two objective run.

3.2 Comparison to Other Lattices

In addition to comparing the optimized and standard IWP TPxS using voxel based FEA in MATLAB that is shown in Figures 7 and 11, we compare the optimized designs against four additional lattices that share the same topology using nTopology's FEA package. For this analysis, we use the Pareto optimal designs, not the sub-optimal fitting found in Section 3.1. We compare against the standard BCC lattice (shown in Figure 1a) as a baseline, and three optimized BCC lattices (shown

[2] https://github.com/jwf23/Optimized_IWP_TPxS

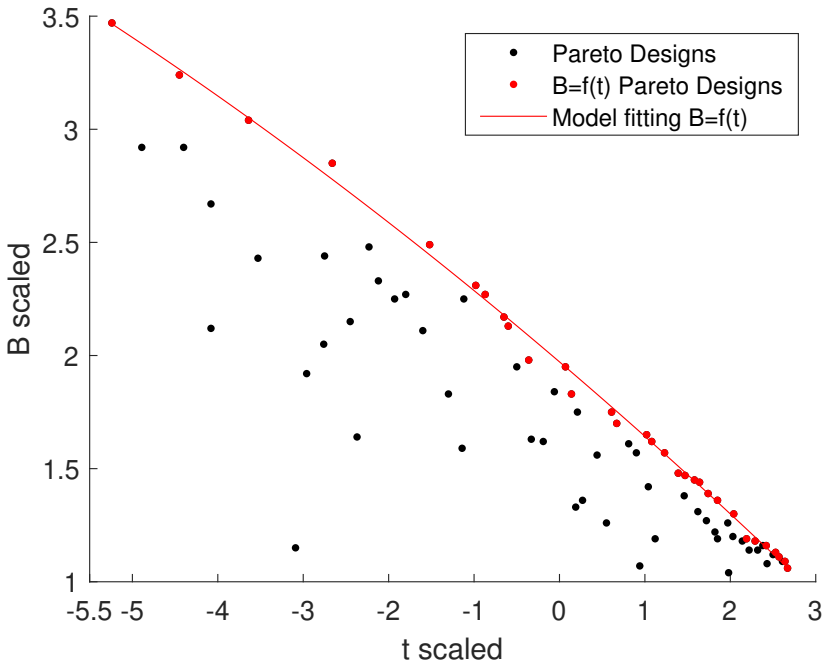

Figure 10: Down-selection of designs in the scaled *B*-*t* space for fitting $B = f(t)$ using Pareto optimality and maximization of the scaled B and t values. Showing the polynomial fit to the Pareto front.

in Figure 4) for a range of volume fractions. We discuss the definition of the FEA models used in Section 2.5 and summarized in Table 1.

Visual comparisons between the different versions of the BCC and our optimized designs like those shown in Figures 12 and 13 highlight the difference in performance at low volume fractions, however at high volume fractions it visually unclear which version out performs and to what degree. To quantify the difference, we evaluate the standard BCC, Wang optimized BCC, and Zhao optimized BCC lattices at nine volume fractions matching volume fractions of the optimized IWP TPxS across the range of volume fractions. For the Lee optimized BCC, we compare to the nearest value from the optimized designs as both exist only at discrete volume fractions. These data as well as the percent difference between the compliance analog for each run and the optimized IWP TPxS are presented in Tables 2 and 3. From the tabulated data, it is clear that the Pareto optimized IWP TPxS shows improvement over the other designs across the full range of volume fractions with one exception. At a volume fraction of 0.1089 it is outperformed by the optimized BCC with rounds between the struts from Wang et al. [8], addressing RQ2.

The lattice in Zhao et al. [19] was optimized for a more limited range of volume fractions compared to this work. As a result, at larger volume fractions the performance is worse than the other designs, which can be seen in Table 2. At volume fractions of 0.4, 0.5, 0.6, 0.7, and 0.8, the Lee optimized BCC exhibits a change of topology caused by multiple minima along the Bézier curve that is used to define the struts [18]. This results in the struts intersecting away from the nodes of the lattice, ultimately changing the topology. Because of this new topology, these lattices are not directly comparable to those in this study and have therefore been omitted. Table 3 contains

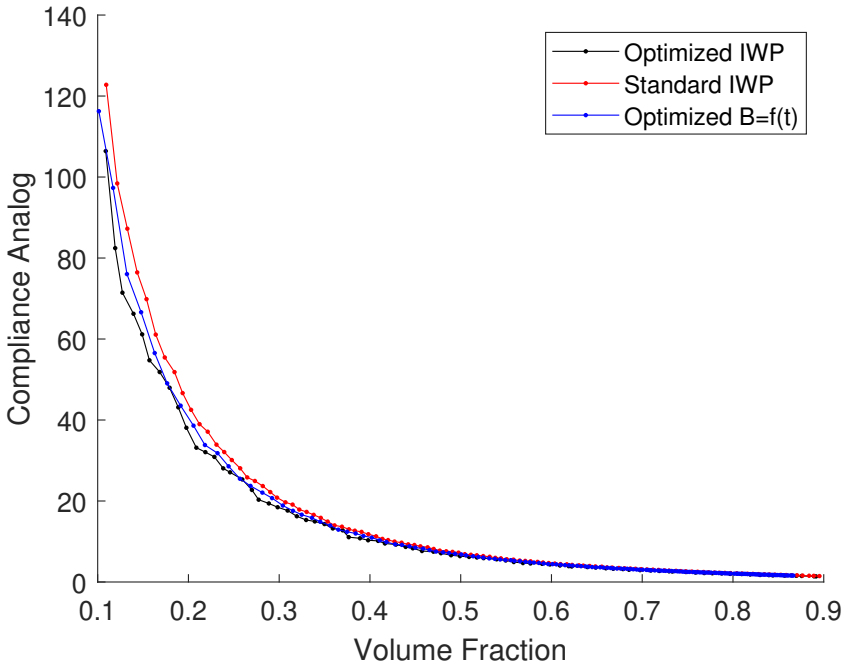

Figure 11: Comparison between the $B = f(t)$ designs, Pareto optimal, and standard IWP TPxS. The B-f(t) designs outperform the standard IWP TPxS. However, they fail to achieve the same performance as the optimized IWP TPxS.

the three volume fractions: 0.1734, 0.2, and 0.3 for which the Lee optimized BCC exhibits the intended topology.

3.3 Geometric Comparison to Standard IWP TPxS

To highlight spatial differences between the geometry of the standard and optimized IWP TPxS, we perform Boolean subtractions between the two at the same volume fractions ($\pm 1\%$) such that all material that is contained in one lattice but not the other can be identified. We show this comparison for five volume fractions in Figure 14. The color indicates which of the structures the different regions of "additional volume" are a part of. We see a trend in the optimized designs of material being drawn away from the "nodes" (at the corners and center of the cell) and moved toward the mid-span of the "beams". This trend aligns intuitively with the initial FEA of the IWP TPxS, shown in Figure 1d, where the stress is minimal at the "nodes". The one exception to the trend occurs at a volume fraction of 0.8925, and is shown in the last row of Figure 14. This is the largest volume fraction on the Pareto frontier and the only design where the relative weighting of the second term (coefficient B) of Equation 2 is lower than the standard in Equation 1.

3.4 Homogenization and Anisotropy Comparison

Although the optimization of the IWP TPxS lattice we performed did not consider the response of the lattice in other directions or the anisotropy. Because in application the loading conditions will be more complex than uniaxial compression, understanding the directional response and anisotropy is useful. The IWP TPxS is highly anisotropic at low volume fractions [13]. To visualize and quantify

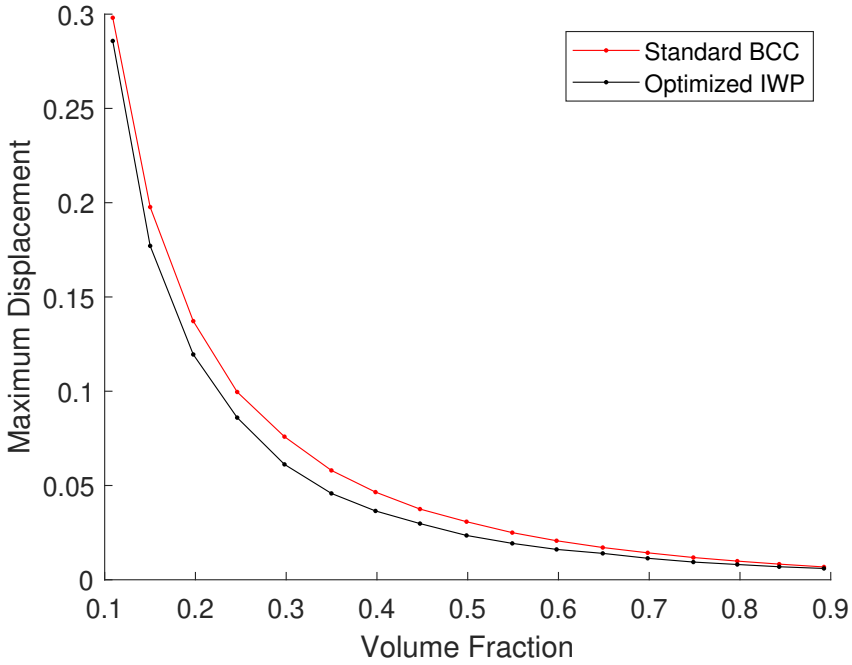

Figure 12: Comparison of the Pareto optimal designs to the strut-based BCC lattice analyzed in nTopology. Showing that our optimized lattices outperforms the standard BCC across the range of volume fractions considered.

the directional response and anisotropy, we can apply linear elastic homogenization based on the methods of Dong, Tang, and Zhao [21], and visualize the Young's Modulus surface at volume fractions of 10.89%, 19.76%, and 29.81%, which we show in Figure 15. From the elements of the homogenized constitutive matrices (C_{ij}), we compute the Zener ratio using Equation 15, which is a measure of the anisotropy of cubic crystals [30]:

$$Z = \frac{2C_{44}}{C_{11} - C_{12}} \tag{15}$$

Compared to the standard IWP TPxS at the same volume fraction, the optimization increases all non-zero elements of the constitutive matrices by the percentages shown in Table 4. From this, we find that the Young's modulus increases in all directions, but the anisotropy also increases slightly in the optimized designs because the difference between the standard and optimized is not uniform for each element of the homogenized constitutive matrices.

4 Conclusions

Lattice structures in additive manufacturing offer a significant opportunity to reduce the weight of components without lose of structural integrity. The implementation of lattice structures can be further improved though the optimization of lattice structures, first at the unit cell level and then at the component level. The workflow of the optimization of the IWP TPxS for a single load case has

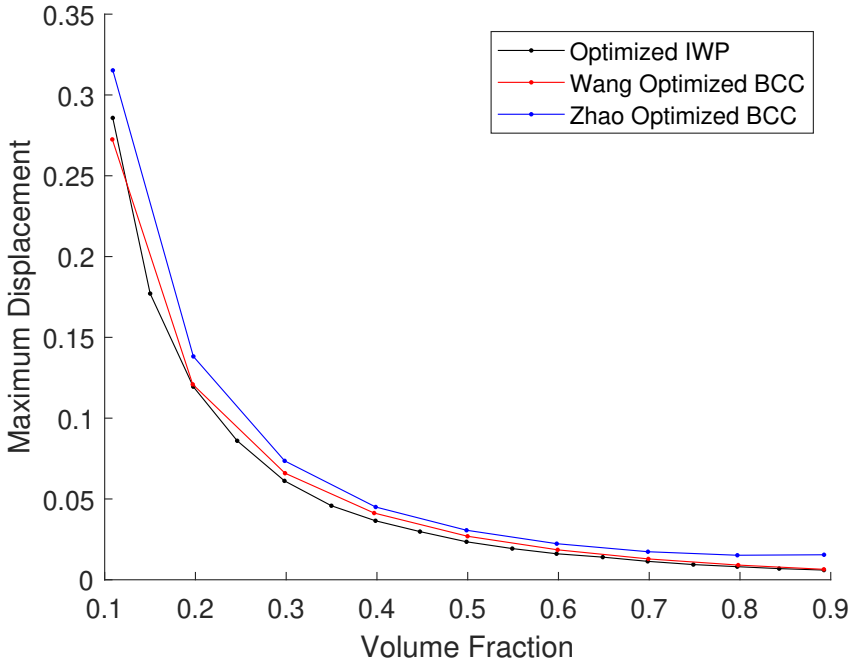

Figure 13: Comparison of the Pareto optimal designs to the optimized BCC lattices generated by Wang et al. [8] and Zhao et al. [19] analyzed in nTopology. Showing that our optimized lattices outperform the optimized BCC designs with one exception at a volume fraction of 0.1089.

been demonstrated and the resulting designs have been available as easy to use blocks importable to nTopology.

In this work we have demonstrated an approach to the optimization of TPMS-based lattices for the IWP TPxS using the Borg MOEA to minimize compliance and volume fraction. We share the results as blocks that can be imported into nTopology for lattice generation. In Section 1, we pose three research questions motivating the optimization of the IWP TPxS, and in Section 3, we present our results pertaining to these questions. We find that improvements over the standard IWP TPxS are possible across a wide range of volume fractions (0.1 to 0.9), addressing our first research question. The sub-question RQ1.1 relates to design space relationships between the Pareto optimal solutions. From the results of our optimization we derive a relationship between the coefficient B and the level set t after fixing $A = 2$. We demonstrated the outperformance of the standard equation; however, the performance of designs on this curve fall short compared to the discrete Pareto optimal designs from Borg. We developed FEA models based on the results of three optimizations of the BCC lattice, as well as the BCC as a baseline. The optimized IWP TPxS outperformed the four variations of the BCC with the exception of the design from Wang et al. [8] which out performed the optimized IWP TPxS at a single volume fraction of 0.1089. Therefore, we find that the optimized IWP TPxS outperforms the BCC designs for most volume fractions tested, but not all (answering RQ 2).

Given the higher stiffness independent of direction, that is shown in Section 3.4, the Pareto optimal lattice replace the standard IWP TPxS in applications where higher stiffness for a given

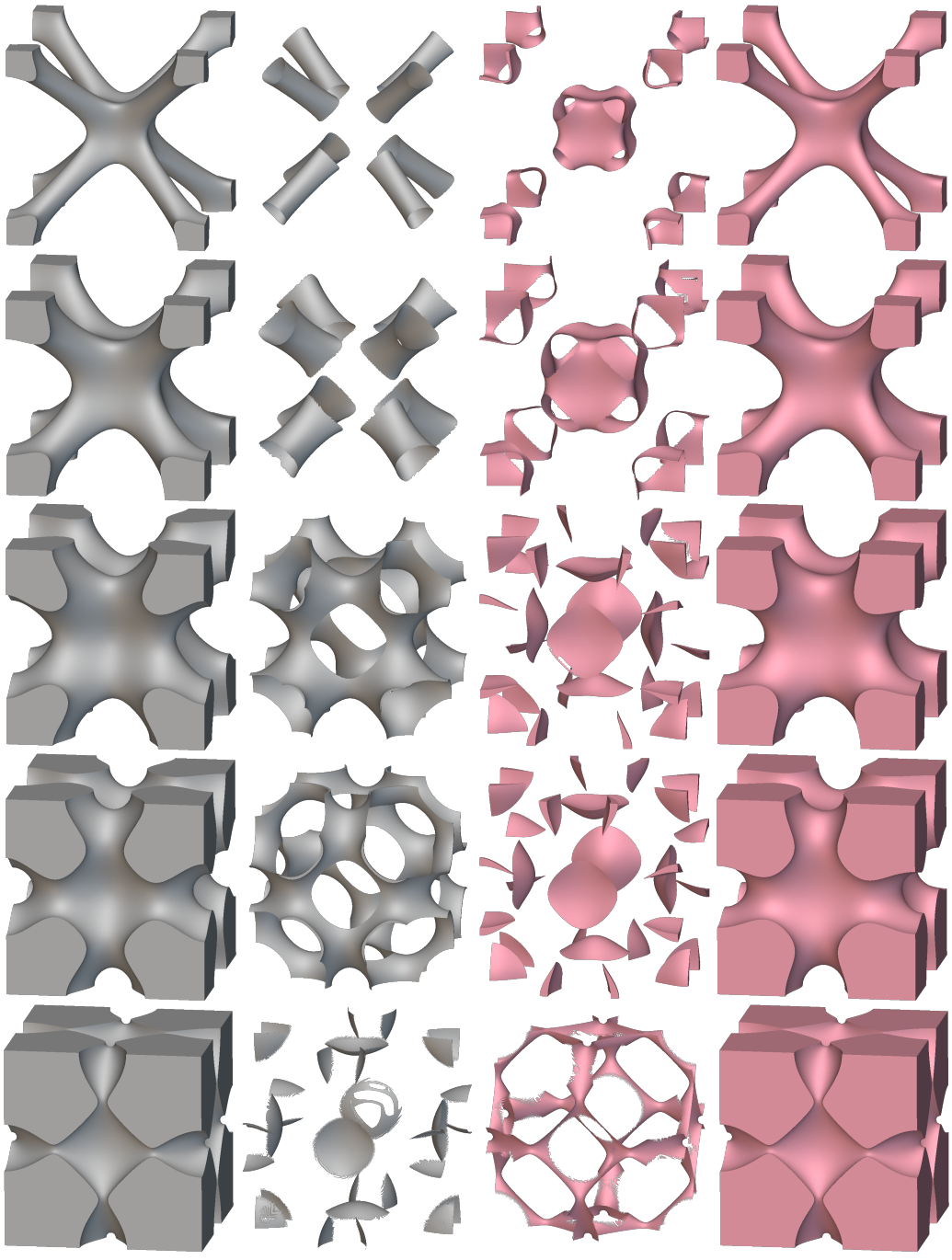

Figure 14: Differences between the optimized IWP TPxS (column a) and standard IWP TPxS (column d) at volume fractions of 0.1089, 0.2460, 0.4987, 0.7481, and 0.8925, from top to bottom. Column b shows the material that is part of the optimized lattice and not part of the standard, and column c shows the opposite. From top to bottom, the percent differences by volume between the two lattices are: 14.6%, 2.2%, 8.2%, 4.8%, and 0.2%. Errors in rendering of thin sections are seen in columns b and c.

weight is desired and in applications where smooth grading of the lattice is needed. The sub-optimal $B = f(t)$ designs can be used in the same manner as the standard IWP TPxS.

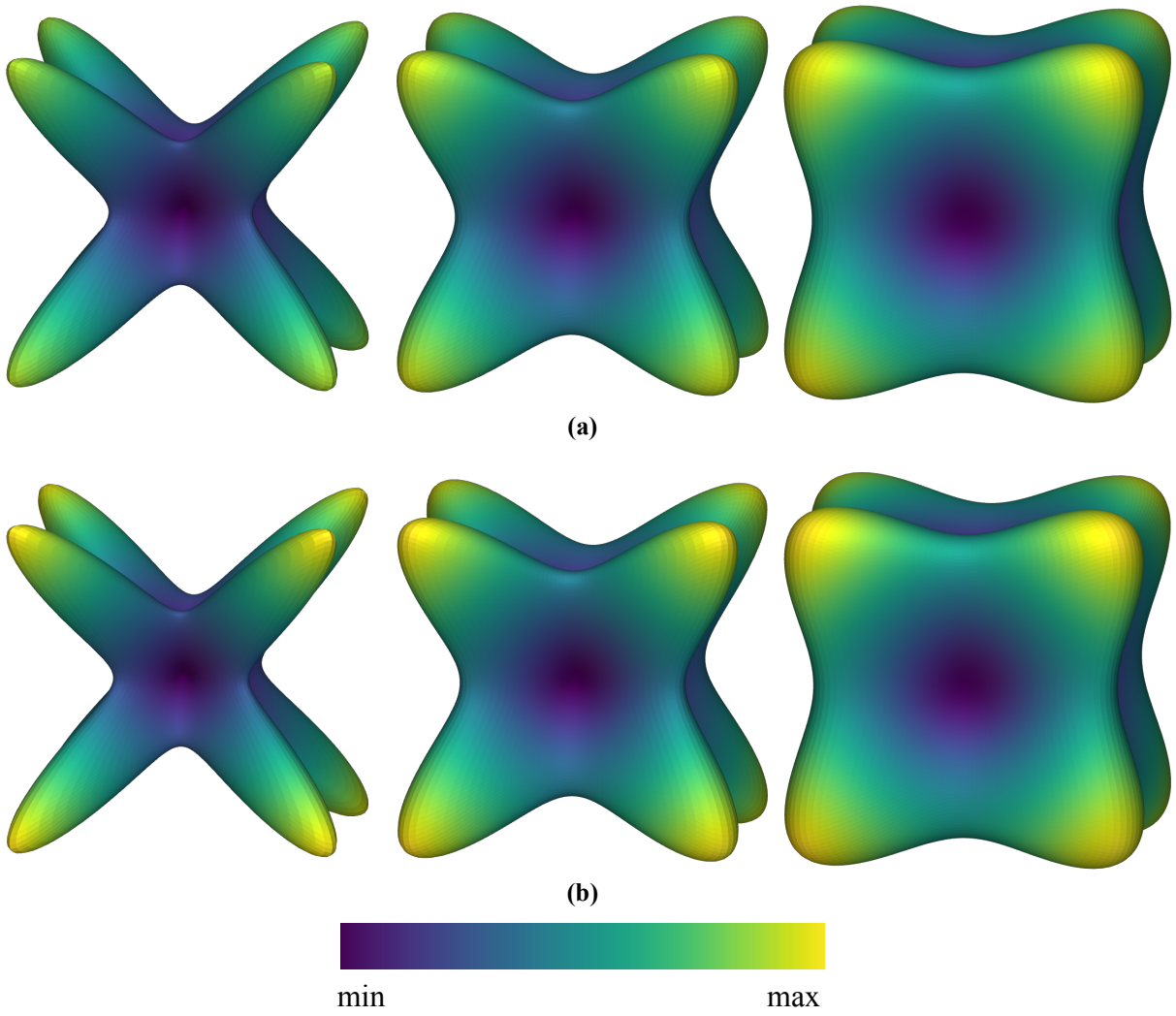

Figure 15: Young's modulus surfaces for (a) the standard IWP TPxS and (b) the optimized IWP TPxS at volume fractions of 0.1089, 0.1976, and 0.2981 from left to right. The respective Zener ratios are: 10.4 and 11.3 (left), 4.84 and 5.15 (middle), and 2.85 and 2.89 at (right). The range of the color bar is normalized for each volume fraction (column) to highlight the differences between the two designs.

We propose four extensions of this work to expand the impact of our results. First, the blending of neighboring unit cells of different, discrete volume fractions should be explored, similar to work performed by Maskery et al. [5]. This technique would offer the ability to use multiple Pareto optimal volume fractions without sharp step changes in geometry at the interfaces. Second, our optimization can form the basis of a larger optimization scheme, where the unit cell is optimized for multiple cases and the results either balanced to produce a globally "optimal" unit cell or used in a component-scale optimization that utilizes optimal unit cells from different loading conditions depending on the local response of the component. Third, application of this optimization method to other TPMS-based lattices including the TPnS and TPSf of the IWP as well as those based on other TPMS. Fourth, application of this optimization approach to equations for the IWP and other TPMS with additional coefficients that allow directional changes to the lattice.

Acknowledgements

This material is based on work funded by the Defense Threat Reduction Agency (DTRA) through the Naval Sea Systems Command (NAVSEA) under Contract No. N000024-18-F-6401, Delivery Order 21F8353. The opinions, findings, conclusions, and recommendations expressed in this material are those of the authors and do not necessarily reflect the views of NAVSEA. Nor do they reflect the views of DTRA or collaborators at NAVSEA.

Table 2: Comparison of designs from the Pareto frontier to the standard BCC and optimized BCC versions from Wang et al. [8] and Zhao et al. [19].

Optimized IWP TPxS		BCC			Wang Optimized BCC			Zhao Optimized BCC		
VF	Deflection	VF	Deflection	Difference	VF	Deflection	Difference	VF	Deflection	Difference
0.1089	0.28577	0.1089	0.29811	4.14%	0.1084	0.27311	-4.63%	0.1090	0.31523	9.35%
0.1976	0.11946	0.1976	0.13718	12.91%	0.1970	0.12093	1.22%	0.1977	0.13821	13.56%
0.2981	0.06125	0.2981	0.07594	19.34%	0.2987	0.06594	7.12%	0.2983	0.07358	16.76%
0.3984	0.03650	0.3984	0.04648	21.48%	0.3969	0.04129	11.61%	0.3986	0.04502	18.93%[3]
0.4987	0.02348	0.4987	0.03075	23.65%	0.4998	0.02693	12.79%	0.4987	0.03064	23.36%[3]
0.5979	0.01612	0.5979	0.02074	22.25%	0.5991	0.01853	13.01%	0.5981	0.02232	27.76%[3]
0.6983	0.01140	0.6983	0.01428	20.15%	0.6990	0.01290	11.64%	0.6986	0.01735	34.28%[3]
0.7970	0.00814	0.7970	0.00987	17.54%	0.7980	0.00909	10.47%	0.7971	0.01517	46.38%[3]
0.8925	0.00599	0.8925	0.00679	11.83%	0.8924	0.00646	7.26%	0.8926	0.01547	61.29%[3]

[3]These volume fraction values fall outside the range for which the lattice was optimized.

Table 3: Comparison of designs from the Pareto frontier to the optimized BCC from Lee, Zhang, and Gu [18]. Fewer values are compared because of topological changes at higher volume fractions.

Optimized IWP TPxS		Lee Optimized		
VF	Deflection	VF	Deflection	Difference
0.1792	0.13547	0.1757	0.16981	20.22%
0.1976	0.11946	0.1961	0.15611	23.47%
0.2981	0.06125	0.2998	0.06867	10.81%

Table 4: The percent increase in the three unique members of the homogenized constitutive matrix from the standard to the optimized IWP TPxS at three volume fractions.

VF	C_{11}	C_{12}	C_{44}
0.1089	13.14%	15.00%	11.45%
0.2981	7.05%	10.45%	5.14%
0.3984	4.04%	6.63%	1.79%

References

[1] Martin Kumke et al. “Methods and tools for identifying and leveraging additive manufacturing design potentials”. In: *International Journal on Interactive Design and Manufacturing (IJIDeM)* 12 (2018), pp. 481–493.

[2] Asliah Seharing, Abdul Hadi Azman, and Shahrum Abdullah. “A review on integration of lightweight gradient lattice structures in additive manufacturing parts”. In: *Advances in Mechanical Engineering* 12.6 (2020), p. 1687814020916951.
[3] Chen Pan, Yafeng Han, and Jiping Lu. “Design and optimization of lattice structures: A review”. In: *Applied Sciences* 10.18 (2020), p. 6374.
[4] Tobias Maconachie et al. “SLM lattice structures: Properties, performance, applications and challenges”. In: *Materials & Design* (2019), p. 108137.
[5] I Maskery et al. “Effective design and simulation of surface-based lattice structures featuring volume fraction and cell type grading”. In: *Materials & Design* 155 (2018), pp. 220–232.
[6] Oraib Al-Ketan, Reza Rowshan, and Rashid K Abu Al-Rub. “Topology-mechanical property relationship of 3D printed strut, skeletal, and sheet based periodic metallic cellular materials”. In: *Additive Manufacturing* 19 (2018), pp. 167–183.
[7] Dhruv Bhate. “Four questions in cellular material design”. In: *Materials* 12.7 (2019), p. 1060.
[8] Xiaoyang Wang et al. “Optimization of graded filleted lattice structures subject to yield and buckling constraints”. In: *Materials & Design* 206 (2021), p. 109746.
[9] Ryan M Latture et al. “Effects of nodal fillets and external boundaries on compressive response of an octet truss”. In: *Acta Materialia* 149 (2018), pp. 78–87.
[10] HG Von Schnering and R Nesper. “Nodal surfaces of Fourier series: fundamental invariants of structured matter”. In: *Zeitschrift für Physik B Condensed Matter* 83.3 (1991), pp. 407–412.
[11] Miao Zhao et al. “Improved mechanical properties and energy absorption of BCC lattice structures with triply periodic minimal surfaces fabricated by SLM”. In: *Materials* 11.12 (2018), p. 2411.
[12] Fabian Günther et al. “Design procedure for triply periodic minimal surface based biomimetic scaffolds”. In: *Journal of the Mechanical Behavior of Biomedical Materials* 126 (2022), p. 104871.
[13] Joseph W. Fisher et al. “Catalog of Triply Periodic Minimal Surfaces, Equation-Based Lattice Structures, and Their Homogenized Property Data”. In: *Data in Brief* (2023), p. 109311.
[14] Dawei Li et al. “Optimal design and modeling of gyroid-based functionally graded cellular structures for additive manufacturing”. In: *Computer-Aided Design* 104 (2018), pp. 87–99.
[15] Dawei Li et al. “Design and optimization of graded cellular structures with triply periodic level surface-based topological shapes”. In: *Journal of Mechanical Design* 141.7 (2019).
[16] Oraib Al-Ketan and Rashid K Abu Al-Rub. “Multifunctional Mechanical Metamaterials Based on Triply Periodic Minimal Surface Lattices”. In: *Advanced Engineering Materials* 21.10 (2019), p. 1900524.
[17] Bradley Hanks and Mary Frecker. “3d additive lattice topology optimization: a unit cell design approach”. In: *International Design Engineering Technical Conferences and Computers and Information in Engineering Conference*. Vol. 84003. American Society of Mechanical Engineers. 2020, V11AT11A028.
[18] Sangryun Lee, Zhizhou Zhang, and Grace X Gu. “Generative machine learning algorithm for lattice structures with superior mechanical properties”. In: *Materials Horizons* 9.3 (2022), pp. 952–960.
[19] Miao Zhao et al. “Design, mechanical properties, and optimization of BCC lattice structures with taper struts”. In: *Composite Structures* (2022), p. 115830.

[20] Dawei Li et al. “Comparison of mechanical properties and energy absorption of sheet-based and strut-based gyroid cellular structures with graded densities”. In: *Materials* 12.13 (2019), p. 2183.
[21] Guoying Dong, Yunlong Tang, and Yaoyao Fiona Zhao. “A 149 Line Homogenization Code for Three-Dimensional Cellular Materials Written in MATLAB”. In: *Journal of Engineering Materials and Technology* 141.1 (2019). DOI: 10.1115/1.4040555.
[22] Yiqiang Wang et al. “Design of graded lattice structure with optimized mesostructures for additive manufacturing”. In: *Materials & Design* 142 (2018), pp. 114–123.
[23] Carlos A Coello Coello, Gary B Lamont, David A Van Veldhuizen, et al. *Evolutionary algorithms for solving multi-objective problems*. Vol. 5. Springer, 2007.
[24] Thomas Lewiner et al. “Efficient implementation of marching cubes’ cases with topological guarantees”. In: *Journal of graphics tools* 8.2 (2003), pp. 1–15.
[25] Gary M Stump. “Multi-Criteria Design Optimization Using Multi-Dimensional Data Visualization”. PhD thesis. Pennsylvania State University, 2004.
[26] Nitish Tripathi. *Plot a plane from 3 points*. 2013. URL: https://www.mathworks.com/matlabcentral/fileexchange/41937-plot-a-plane-from-3-points.
[27] Meinhard Wohlgemuth et al. “Triply periodic bicontinuous cubic microdomain morphologies by symmetries”. In: *Macromolecules* 34.17 (2001), pp. 6083–6089.
[28] Ian Maskery et al. “Insights into the mechanical properties of several triply periodic minimal surface lattice structures made by polymer additive manufacturing”. In: *Polymer* 152 (2018), pp. 62–71.
[29] David Hadka and Patrick Reed. “Borg: An Auto-Adaptive Many-Objective Evolutionary Computing Framework”. In: *Evolutionary Computation* 21.2 (2013), pp. 231–259.
[30] Clarence Zener. “Contributions to the theory of beta-phase alloys”. In: *Physical Review* 71.12 (1947), p. 846.

Appendix A

Our Borg optimization described in Section 2, resulted in 80 designs along the Pareto frontier of the optimized IWP lattice. The volume fraction and compliance analog objectives are tabulated alongside points of similar volume fraction from the standard IWP and the percent difference between the compliance analogs for each. The percent difference shows that, even at a slight volume fraction disadvantage, the optimized design outperforms the standard across the frontier.

Table A1: All points on the Pareto Frontier for the optimized IWP lattice and associated points from the standard IWP dataset shown in Figure 7.

Optimized IWP		Standard IWP		
VF	Compliance Analog	VF	Compliance Analog	Percent Difference
0.1089	106.407	0.1094	122.777	13.3%
0.1193	82.447	0.1216	98.424	16.2%
0.1273	71.439	0.1327	87.241	18.1%
0.1395	66.233	0.1435	76.450	13.4%
0.1490	61.150	0.1538	69.847	12.5%
0.1570	54.750	0.1640	61.087	10.4%
0.1683	51.846	0.1739	55.446	6.5%
0.1792	47.964	0.1847	51.831	7.5%
0.1888	43.133	0.1936	46.647	7.5%
0.1977	38.084	0.2029	42.515	10.4%
0.2087	33.161	0.2122	38.979	14.9%
0.2187	32.068	0.2212	37.110	13.6%
0.2286	30.887	0.2309	33.914	8.9%
0.2383	28.062	0.2394	32.092	12.6%
0.2459	27.084	0.2478	30.113	10.1%
0.2594	25.328	0.2648	25.830	1.9%
0.2699	22.732	0.2732	24.946	8.9%
0.2774	20.321	0.2819	23.692	14.2%
0.2886	19.398	0.2902	22.208	12.7%
0.2983	18.460	0.3069	19.677	6.2%
0.3093	17.642	0.3148	19.116	7.7%
0.3194	16.234	0.3221	17.885	9.2%
0.3297	15.311	0.3302	17.302	11.5%
0.3392	14.956	0.3458	15.843	5.6%
0.3499	14.305	0.3534	14.922	4.1%
0.3591	13.223	0.3610	13.982	5.4%
0.3700	12.755	0.3768	13.013	2.0%
0.3766	11.071	0.3768	13.013	14.9%
0.3890	10.795	0.3907	12.376	12.8%
0.3980	10.306	0.3982	11.803	12.7%
0.4090	10.151	0.4137	10.643	4.6%
0.4165	9.513	0.4200	10.353	8.1%
0.4287	9.247	0.4348	9.707	4.7%
0.4393	8.662	0.4421	9.299	6.8%
0.4472	8.319	0.4490	9.139	9.0%
0.4573	7.650	0.4636	8.562	10.6%
0.4699	7.481	0.4702	8.158	8.3%
0.4782	7.110	0.4840	7.587	6.3%
0.4894	6.611	0.4910	7.438	11.1%
0.4992	6.384	0.5045	6.871	7.1%
0.5092	6.191	0.5112	6.721	7.9%
0.5178	6.050	0.5248	6.403	5.5%
0.5252	5.883	0.5319	6.231	5.6%
0.5395	5.601	0.5443	5.845	4.2%
0.5496	5.318	0.5507	5.616	5.3%
0.5585	4.931	0.5649	5.291	6.8%
0.5686	4.674	0.5711	5.211	10.3%
0.5768	4.576	0.5770	5.109	10.4%
0.5896	4.493	0.5907	4.810	6.6%
0.5983	4.335	0.6037	4.549	4.7%
0.6093	4.072	0.6099	4.421	7.9%
0.6190	3.908	0.6227	4.213	7.2%
0.6223	3.830	0.6227	4.213	9.1%
0.6397	3.683	0.6421	3.950	6.8%
0.6486	3.562	0.6554	3.776	5.7%
0.6599	3.384	0.6611	3.602	6.0%
0.6681	3.265	0.6742	3.457	5.6%
0.6788	3.189	0.6806	3.383	5.7%
0.6854	3.025	0.6869	3.324	9.0%
0.6976	2.926	0.6989	3.169	7.7%
0.7092	2.832	0.7118	3.042	6.9%
0.7189	2.726	0.7244	2.859	4.7%
0.7297	2.634	0.7297	2.801	6.0%
0.7333	2.581	0.7373	2.753	6.3%
0.7481	2.466	0.7545	2.570	4.1%
0.7588	2.325	0.7610	2.532	8.2%
0.7684	2.212	0.7730	2.395	7.6%
0.7773	2.155	0.7796	2.325	7.3%
0.7875	2.113	0.7911	2.245	5.9%
0.7969	2.003	0.7974	2.198	8.9%
0.8096	1.966	0.8100	2.082	5.6%
0.8190	1.857	0.8219	1.999	7.1%
0.8298	1.738	0.8347	1.900	8.5%
0.8396	1.700	0.8402	1.856	8.4%
0.8439	1.629	0.8462	1.805	9.7%
0.8570	1.579	0.8586	1.710	7.7%
0.8698	1.524	0.8706	1.650	7.6%
0.8757	1.490	0.8767	1.582	5.8%
0.8894	1.398	0.8953	1.457	4.0%
0.8916	1.380	0.8953	1.457	5.3%

Continued